

Chemo-dynamics and asteroseismic ages of seven metal-poor red giants from the Kepler field

Arthur Alencastro Puls,^{1,5}★ Luca Casagrande,^{1,5} Stephanie Monty,^{1,5} David Yong,^{1,5} Fan Liu,² Dennis Stello,^{3,4,5} Victor Aguirre Børsen-Koch,⁴ and Ken C. Freeman^{1,5}

¹Research School of Astronomy and Astrophysics, Australian National University, Canberra, ACT 2611, Australia

²Centre for Astrophysics and Supercomputing, Swinburne University of Technology, Melbourne, VIC 3122, Australia

³School of Physics, University of New South Wales, Sydney, NSW 2052, Australia

⁴Stellar Astrophysics Centre (SAC), Department of Physics and Astronomy, Aarhus University, Ny Munkegade 120, DK-8000 Aarhus C, Denmark

⁵ARC Centre of Excellence for All Sky Astrophysics in 3 Dimensions (ASTRO3D), Australia

Accepted 2021 November 30. Received 2021 November 14; in original form 2021 September 5

ABSTRACT

In this work we combine information from solar-like oscillations, high-resolution spectroscopy and Gaia astrometry to derive stellar ages, chemical abundances and kinematics for a group of seven metal-poor Red Giants and characterise them in a multidimensional *chrono-chemo-dynamical* space. Chemical abundance ratios were derived through classical spectroscopic analysis employing 1D LTE atmospheres on Keck/HIRES spectra. Stellar ages, masses and radii were calculated with grid-based modelling, taking advantage of availability of asteroseismic information from Kepler. The dynamical properties were determined with Galpy using Gaia EDR3 astrometric solutions. Our results suggest that underestimated parallax errors make the effect of Gaia parallaxes more important than different choices of model grid or – in the case of stars ascending the RGB – mass-loss prescription. Two of the stars in this study are identified as potentially evolved halo blue stragglers. Four objects are likely members of the accreted Milky Way halo, and their possible relationship with known accretion events is discussed.

Key words: Galaxy: abundances – Galaxy: kinematics and dynamics – stars: fundamental parameters

1 INTRODUCTION

Since the first proposal of Searle & Zinn (1978) the hierarchical formation of the Milky Way (hereafter, the Galaxy), supported by the Λ CDM model (White & Rees 1978; Kobayashi & Nakasato 2011; Planck Collaboration et al. 2016), has been an object of debate and a target of surveys (Gilmore et al. 2012; De Silva et al. 2015; Majewski et al. 2017). One avenue to trace the assembly history of our Galaxy is by using stars, and in particular their kinematics, chemical abundances, ages and spatial distributions.

Signatures of the formation and evolution of our Galaxy lie in the chemical compositions of stars (e.g., Venn et al. 2004). One key abundance ratio is $[\alpha/\text{Fe}]$, which provides a measure of the star formation history for the following reason. The α elements are primarily produced in massive stars that explode as Type II supernovae (SNe) on short timescales (10^7 years) whereas Fe is produced in Type Ia SNe on longer timescales ($\sim 10^9$ years) (e.g., Tinsley 1979; Matteucci & Greggio 1986; McWilliam 1997). This abundance ratio has thus provided key constraints on the relative star formation histories of the thin disk, thick disk, halo, bulge and dwarf galaxies (e.g., Freeman & Bland-Hawthorn 2002; Tolstoy et al. 2009).

The history of our Galaxy can also be traced using stellar kinematics. After the second data release of the Gaia mission (Gaia Collaboration et al. 2018) it has become increasingly clear that a

massive dwarf galaxy merged with our Galaxy at $z \sim 3$, which is consistent with the hierarchical formation hypothesis from Λ CDM. The signature of that merger was only detected through the combination of precise distances and kinematics from Gaia and chemical abundances from spectroscopy (Belokurov et al. 2018; Haywood et al. 2018; Myeong et al. 2018; Helmi 2020).

It is also clear that, in addition to stellar chemical abundances and kinematics, a more detailed understanding of the evolution of our Galaxy requires accurate stellar ages. Until recently, however, accurate stellar ages have been difficult to obtain (Soderblom 2010; Chaplin et al. 2011). In the case of red giant stars, masses are a good proxy for ages, as most of the stellar lifetime is spent in the main sequence, before they evolve to the (relatively) short red giant phase (Kippenhahn et al. 2012). Recently, exquisite photometric data collected by space-based missions such as Kepler (Koch et al. 2010), K2 (Howell et al. 2014), CoRoT (Baglin et al. 2006) and TESS (Ricker et al. 2014) have allowed us to derive stellar radii, masses and ages with precision of a few percent (Casagrande et al. 2016; Anders et al. 2017; Silva Aguirre et al. 2018, 2020; Zinn et al. 2021). Red giant stars display solar-like oscillations in their power spectra, which are characterised by a Gaussian envelope centered at the frequency of maximum power ν_{max} and peaks separated by the average frequency spacing $\Delta\nu$ between consecutive orders of same angular degree (Chaplin & Miglio 2013; Hekker & Christensen-Dalsgaard 2017). It can be shown that these asteroseismic quantities are proportional to fundamental stellar properties such as average

★ E-mail: arthur.alencastropuls@anu.edu.au (AAP)

density, effective temperature and surface gravity, and, assuming that these proportionality relations can be scaled to the solar values, they can be rewritten as (Ulrich 1986; Brown et al. 1991; Kjeldsen & Bedding 1995),

$$\frac{M}{M_{\odot}} \simeq \left(\frac{\nu_{\max}}{\nu_{\max, \odot}} \right)^3 \left(\frac{\Delta\nu}{\Delta\nu_{\odot}} \right)^{-4} \left(\frac{T_{\text{eff}}}{T_{\text{eff}, \odot}} \right)^{1.5}, \quad (1)$$

and,

$$\frac{R}{R_{\odot}} \simeq \left(\frac{\nu_{\max}}{\nu_{\max, \odot}} \right) \left(\frac{\Delta\nu}{\Delta\nu_{\odot}} \right)^{-2} \left(\frac{T_{\text{eff}}}{T_{\text{eff}, \odot}} \right)^{0.5}, \quad (2)$$

and also,

$$\log g \simeq \log \left(\frac{\nu_{\max}}{\nu_{\max, \odot}} \right) + 0.5 \log \left(\frac{T_{\text{eff}}}{T_{\text{eff}, \odot}} \right) + \log g_{\odot}, \quad (3)$$

where M and R are, respectively, stellar mass and radius, T_{eff} is the effective temperature, and g is the surface gravity. Recent studies have shown that, in the case of stars ascending the Red Giant Branch (RGB), Eqs. (1) and (2) tend to overestimate masses and, by a smaller extent, also radii, and a small non-linear correction would be required for them (e.g., Miglio et al. 2016; Gaulme et al. 2016; Rodrigues et al. 2017; Brogaard et al. 2018), however the results from Zinn et al. (2019b, 2020) are in agreement with radii derived from Gaia DR2 observations (Gaia Collaboration et al. 2018) at the 2% level.

The prospect of combining stellar ages, kinematics and chemical abundance patterns is now a reality (e.g., Montalbán et al. 2021; Verma et al. 2021). The goal of this paper is to combine stellar ages, chemical abundances and kinematics to further explore the formation and evolution of our Galaxy and to better understand the limitations and prospects of this approach. In Section 2 we describe sample selection, observations and data reduction. Section 3 outlines the methods employed in the analysis, while in Section 4 possible sources of age systematics are discussed. Results are presented in Section 5, and Section 6 contains our final remarks.

2 OBSERVATIONS AND DATA REDUCTION

The sample used in this work is composed of seven red giant stars in the *Kepler* field whose previous asteroseismic estimates of masses/ages do not appear consistent with their chemical abundance ratios. Five of them are from the first APOKASC catalog (Pinsonneault et al. 2014), and were originally studied by Epstein et al. (2014), who derived asteroseismic masses larger than expected by the authors for metal-poor, halo stars. The other two are from SAGA (Casagrande et al. 2014), whose results also suggest young ages for metal-poor stars (e.g., stellar mass of $1.07 M_{\odot}$ and $[\text{Fe}/\text{H}] = -2.44$ in case of KIC 4671239). Table 1 presents their values for $\Delta\nu$ and ν_{\max} adopted from the literature. Their position along the RGB can be inspected in Fig. 1 through their respective ν_{\max} values.

These stars were observed with HIRES at W. M. Keck Observatory (Vogt et al. 1994) with the goal of deriving a complete chemical inventory to provide nucleosynthetic checks on ages (program ID: Z079Hr, Casagrande 2016). The raw data were reduced using the Mauna Kea Echelle Extraction (MAKEE) data reduction pipeline, including bias subtraction, flat-fielding, optimal extraction of spectra and wavelength calibration (heliocentric velocity corrected). The individual reduced spectra were radial-velocity corrected, co-added

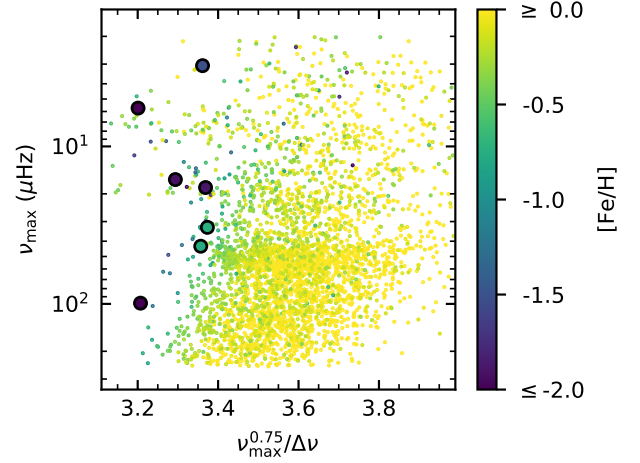


Figure 1. Asteroseismic diagram showing program stars (circles) compared to the subsample of RGB stars from APOKASC-2 (Pinsonneault et al. 2018, points).

and normalised using IRAF¹. The combined signal-to-noise-ratio (S/N) of the spectra ranges from 60 to 170 at $\lambda \approx 590$ nm, while the nominal spectral resolution is $\lambda/\Delta\lambda = 47,700$. Wavelength coverage is 420-850 nm, with a gap in the 530-550 nm region.

3 ANALYSIS

The stellar parameters in this work were derived combining different methods run in several iterations: the classical spectroscopic method (see, e.g., Jofré et al. (2019) for a comprehensive review), the InfraRed Flux Method (IRFM, Blackwell & Shallis 1977) and asteroseismic grid-based modelling (GBM, Stello et al. 2009). Spectroscopy allows us to find the detailed chemical composition of a star, while the knowledge of $\Delta\nu$ and ν_{\max} enables the possibility of deriving masses with good precision, which then can be converted into ages for an assumed set of isochrones.

3.1 Fundamental parameters and chemical abundances

For the spectroscopic component of the analysis we have employed solar-scaled 1D LTE Kurucz models interpolated from a grid (Castelli & Kurucz 2003). Initially, the equivalent widths (EW) of Fe I and Fe II were measured through Gaussian fitting in selected weak lines compiled from the literature and using $\log gf$ values from NIST² (Cayrel et al. 2004; Alves-Brito et al. 2010; Meléndez et al. 2012; Barbay et al. 2013; Ishigaki et al. 2013; Yong et al. 2014, see Table 2 for the line list) and used as input to find the four atmospheric model parameters with the 2017 version of MOOG (Snedden 1973). Effective temperatures (T_{eff}) and surface gravity values (in terms of $\log g$) were obtained by imposing excitation and ionisation balance, respectively, for each star. The value for the microturbulent velocity (ν_t) is found eliminating any correlation between Fe I line strengths – given by

¹ IRAF is distributed by the National Optical Astronomy Observatory, which is operated by the Association of Universities for Research in Astronomy, Inc., under cooperative agreement with the National Science Foundation.

² https://physics.nist.gov/PhysRefData/ASD/lines_form.html

Table 1. Program stars, IDs from Epstein et al. (2014), as well as IDs adopted here for SAGA (Casagrande et al. 2014) stars, their adopted average seismic parameters $\Delta\nu_{\text{obs}}$ and ν_{max} , and their sources: (A) Yu et al. (2018), (B) Pinsonneault et al. (2018). Period spacings Π_s from Ting et al. (2018a,b) and Mosser et al. (2018, for KIC 4671239). Both Gaia DR2 and EDR3 parallaxes (Gaia Collaboration et al. 2018, 2021) shown here are corrected according to Zinn et al. (2019a) and Lindegren et al. (2021), respectively.

Star	ID	RA (J2000)	DEC (J2000)	$\Delta\nu_{\text{obs}}$ μHz	ν_{max} μHz	Src	Π_s s	ϖ_{DR2} mas	ϖ_{EDR3} mas
KIC 4345370	H	18 59 35.1716	+39 26 48.895	4.050 ± 0.012	32.66 ± 0.29	A	76.08	0.7693 ± 0.0235	0.6852 ± 0.0105
KIC 4671239	S1	19 43 40.9842	+39 42 44.763	9.782 ± 0.027	98.94 ± 0.44	A	66.60	0.4489 ± 0.0227	0.4136 ± 0.0125
KIC 6279038	S2	19 19 18.1907	+41 39 57.419	1.154 ± 0.021	5.71 ± 0.03	B	...	0.1928 ± 0.0271	0.1898 ± 0.0099
KIC 7191496	A	19 16 07.6460	+42 46 32.003	2.455 ± 0.021	16.23 ± 0.24	A	58.76	0.4718 ± 0.0190	0.3980 ± 0.0113
KIC 8017159	C	19 08 41.6306	+43 52 10.320	0.690 ± 0.017	3.07 ± 0.02	B	...	0.3748 ± 0.0258	0.3217 ± 0.0093
KIC 11563791	D	19 36 52.2056	+49 35 59.379	5.005 ± 0.019	43.03 ± 0.51	A	70.09	1.0271 ± 0.0251	0.9603 ± 0.0102
KIC 12017985	B	19 37 12.0086	+50 24 55.593	2.620 ± 0.018	18.24 ± 0.29	A	63.72	0.8540 ± 0.0269	0.8413 ± 0.0332

Table 2. Adopted line list and equivalent widths measured in this work. Lines fitted through spectral synthesis are indicated in the fifth column. Log gf values are from the NIST database. The complete version of this table is available in the supplementary material.

Wavelength \AA	Species Z.ion	LEP eV	log gf dex	KIC4345370 m \AA	KIC4671239 m \AA	KIC6279038 m \AA	KIC7191496 m \AA	KIC8017159 m \AA	KIC11563791 m \AA	...
6707.76	3.0	0.00	-0.002	Synthesis						
6707.91	3.0	0.00	-0.303	Synthesis						
6300.30	8.0	0.00	-9.720	Synthesis						
6363.78	8.0	0.02	-10.190	Synthesis						
5682.64	11.0	2.10	-0.706	71.9	48.8	...
5688.20	11.0	2.10	-0.452	90.4	59.8	...
6154.23	11.0	2.10	-1.547	24.4
6160.75	11.0	2.10	-1.246	35.2	16.3	...
...

the logarithm of its EW normalized by its wavelength – and the respective Fe I abundances as calculated by MOOG.

The adopted models have solar-scaled composition. To account for α -enhancement, the metallicity, in terms of $[\text{M}/\text{H}]$, was estimated using the formula from Salaris et al. (1993):

$$[\text{M}/\text{H}] = [\text{Fe}/\text{H}] + \log_{10}(0.638 \times 10^{[\alpha/\text{Fe}]} + 0.362) \quad (4)$$

where α is the median of (Mg, Si, Ca). MOOG calculates the abundances from the EW of the individual species, allowing us to estimate the output $[\text{M}/\text{H}]_{(\text{Fe}, \alpha)}$ with Eq. 4. The metallicity is then found iteratively when an atmospheric model yields a $[\text{M}/\text{H}]_{(\text{Fe}, \alpha)}$ that is equal to the input $[\text{M}/\text{H}]_{\text{MODEL}}$. The spectroscopic atmospheric parameters are found when they generate an atmospheric model that satisfies *simultaneously* all the conditions described above – (i) excitation balance, (ii) ionization balance, (iii) absence of correlation between line strength and line abundance and (iv) agreement between input and output $[\text{M}/\text{H}]$.³

For each star, the value of $[\text{Fe}/\text{H}]$ used to estimate $[\text{M}/\text{H}]$ is the median of the abundances taken from its Fe II lines. The adoption of Fe II lines for $[\text{M}/\text{H}]$ has been made due to the large metallicity range of the program stars and the lower sensitivity of Fe II to NLTE effects. However, the small number of measurable Fe II lines (see Table 2) prevents a reliable linear fit to be made between line strengths and abundances and thus we have had to rely on the larger number of Fe I lines for this task. It is known that the $\Delta[\text{Fe}/\text{H}] = [\text{Fe}/\text{H}]_{\text{NLTE}} - [\text{Fe}/\text{H}]_{\text{LTE}}$

is different for each of the individual Fe I lines and this can impact the estimation of ν_t (e.g., Lind et al. 2012; Amarsi et al. 2016). Lind et al. estimated the change in ν_t due to NLTE effects, and from inspection of their fig. 7 we can assume that these effects are very mild in the parameter space of our sample, $|\Delta\nu_t| \rightarrow 0 \text{ km s}^{-1}$. The spectrum of the most metal-poor target, KIC 4671239, shows no Fe II features. In this case, derivation of atmospheric parameters through full ionisation/excitation balance is not possible. ‘Spectroscopic’ atmospheric parameters for KIC 4671239 were derived keeping $[\text{M}/\text{H}]$ fixed at -3 dex and adopting log g from Eq. 3, and their respective uncertainties (shown in Fig. 2) are conservative estimates. We tested two representative stars, KIC 8017159 and KIC 12017985, to check if the adoption of alpha-enhanced models instead of solar-scaled models with Eq. 4 would result in qualitatively distinct results. In both cases, $[\text{X}/\text{H}]$ have consistently shifted by $\delta[\text{X}/\text{H}] \approx -0.08$ dex for the species measured with the EW method, with scatter in $\delta[\text{X}/\text{H}]$ being lower than 0.02 dex. Hence, $[\text{X}/\text{Fe}]$ seems to be unaffected by the choice of models. These two stars were chosen because of their distinct $[\text{Mg}/\text{Fe}]$, the former having $[\text{Mg}/\text{Fe}]$ close to the solar value and the later being Mg-rich (see Section 5 for the results).

With initial values for metallicity calculated using the classical spectroscopic method, we could then estimate T_{eff} for each star using an implementation of the IRFM (Casagrande et al. 2010, 2021). This process was divided in two steps. For the first one, input photometry was taken from published JHKs 2MASS (Cutri et al. 2003) and Gaia DR2 magnitudes (Gaia Collaboration et al. 2018). Reddening was estimated using the 2019 version of Bayestar (Green et al. 2019), interpolated over distances published by Bailer-Jones et al. (2018). The IRFM generates a grid of T_{eff} as function of metallicity and log g and the resulting temperatures were interpolated from this grid

³ Atmospheric parameters convergence was achieved using the MOOG wrapper Xiru, written in Python, available at <https://github.com/arthur-puls/xiru>.

Table 3. The stellar parameters adopted to generate the atmospheric models for the spectroscopic analysis.

Star	T_{eff} K	$\log g$ dex	[M/H] dex	v_t km s^{-1}
KIC 4345370	4804	2.421	-0.61	1.13
KIC 4671239	5295	2.929	-2.55	1.38
KIC 6279038	4880	1.640	-1.73	1.88
KIC 7191496	5088	2.123	-1.79	2.50
KIC 8017159	4688	1.386	-1.46	1.40
KIC 11563791	4913	2.543	-0.70	1.06
KIC 12017985	5075	2.178	-1.65	1.97

using the values calculated with the classical spectroscopic method described above.

Before proceeding to the second step of the IRFM we made a run of the first iteration of GBM employing the version 0.27 of BASTA (Silva Aguirre et al. 2015, 2017; Aguirre Børsen-Koch et al. 2021). We used BASTA to fit a set of observables into a grid of BaSTI isochrones (Hidalgo et al. 2018) to estimate the fundamental parameters of a star using bayesian inference. The following parameters were used as global inputs for the BaSTI isochrones: overshooting (0.2), diffusion (0.0), η mass loss (0.3) and no α -enhancement. The mass loss parameter is still very uncertain (e.g., Miglio et al. 2012; Tailo et al. 2020) and, while the value $\eta=0.3$ was adopted, we also tested the situation when mass-loss is neglected (see Section 4). Meanwhile, α -enhancement was defined as zero because we are scaling metallicity to the solar mixture with Eq. 4.

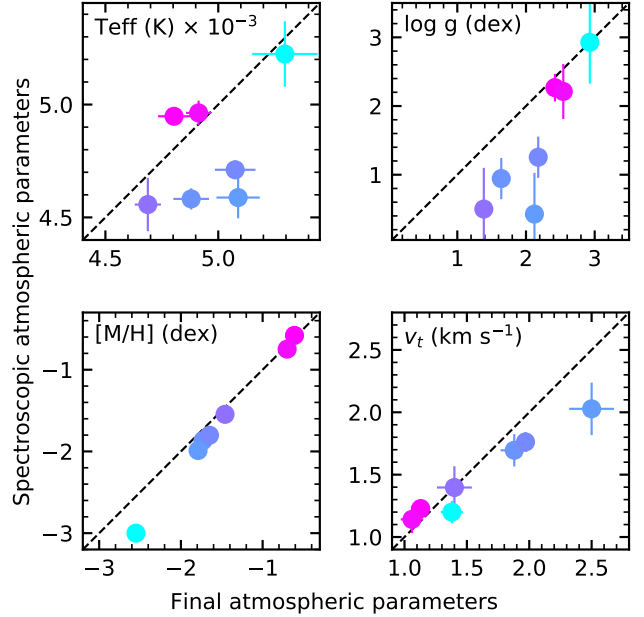
The model-based correction from Serenelli et al. (2017) has been applied for $\Delta\nu$, rescaling this observable though a correction factor $f_{\Delta\nu}$:

$$\Delta\nu_m = \frac{\Delta\nu}{f_{\Delta\nu}} \quad (5)$$

where $\Delta\nu$ represents the value of the large frequency separation for a given star listed in Table 1, while $\Delta\nu_m$ is the value used for BaSTI grid fitting. From Eqs. 1 and 5, the ratio between corrected and uncorrected stellar masses is expected to be $f_{\Delta\nu}^4$, unless further corrections are applied. Typical values of $f_{\Delta\nu}$ range from 0.95 to 1, i.e., the corrected mass can be up to 20% lower than the uncorrected one.

Regarding the individual observables, two sets were chosen: $s_p = (T_{\text{eff}}, [M/H], \Delta\nu, v_{\text{max}}, \text{evolutionary phase}, 2\text{MASS } K_s, \text{parallax})$ and another set without parallax, hereafter called s_n . To inform the prior on evolutionary stage the values of period spacing shown in Table 1 were adopted. All targets in this work with period spacing measurements Π_s have $\Delta\nu < 10 \mu\text{Hz}$ and $\Pi_s < 100$ s. All of them (5 out of 7) can be assumed as being on the RGB (see, e.g. fig. 1 from Mosser et al. 2014). For the remaining stars, KIC 6279038 and KIC 8017159, the evolutionary stage recommended by Yu et al. (2018) was adopted (RGB) for the former, while the later had no evolutionary stage prior defined. Flat priors were adopted for the other observables. The output from GBM yielded current and initial masses, radii, luminosities, ages, $E(B - V)$, distances and $\log g$, as well as fitted values for the input observables. These $\log g$ values, along with the $E(B - V)$ calculated with BASTA, were then used as input in the second iteration of the IRFM.

The second IRFM iteration yielded the T_{eff} values adopted in this work. The median difference from the first to the second iteration is 17 K. The final T_{eff} values replaced those from the first IRFM iteration in a new run of BASTA that yielded the values adopted in

**Figure 2.** Pure spectroscopic parameters as function of respective adopted atmospheric parameters shown in Table 3. Points are color-coded by adopted [M/H]. Dashed lines represent the identity function, while dotted lines show typical uncertainty intervals for the pure spectroscopic set.

this work for the output parameters mass – both the present-day asteroseismically inferred one, and initial one before any mass-loss took place – radius, luminosity, age, $E(B - V)$, distance and $\log g$. The surface gravity and T_{eff} values derived in this last BASTA/IRFM run were employed to calculate the final [M/H] and v_t . Both [M/H] and v_t were calculated in the same way as done in the classical spectroscopic approach, but this time with T_{eff} and $\log g$ kept fixed to IRFM/BASTA values when interpolating the Kurucz models. Table 3 shows the final stellar parameters adopted in this work. In Fig. 2 the atmospheric parameters derived using the classical spectroscopic method are compared with the adopted parameters. The metal-poor stars ($[M/H] < -1$) present the largest deviations between the purely spectroscopic and hybrid⁴ sets of atmospheric parameters.

Using the atmospheric model interpolated from the adopted T_{eff} , $\log g$, [M/H], and v_t , the abundances for each species could be calculated, either by direct curve of growth analysis using the MOOG driver *abfind* or by fitting a synthetic spectrum on the observed one. Species whose lines are subject to hyperfine and/or isotopic splitting, or are known to have non-negligible blends, were measured by spectral synthesis (Li, O, odd-Z Fe-peak, and n-capture elements) by fitting synthetic spectra to the observed ones. The remaining species had their abundances calculated through curve of growth analysis.

3.1.1 Uncertainties

Uncertainties for the atmospheric parameters were estimated as follows: for T_{eff} , a MonteCarlo (MC) was run in the IRFM using uncertainties in the adopted [Fe/H], $\log(g)$, reddening and photometry. The

⁴ Spectroscopic metallicity and microturbulence, with IRFM T_{eff} and asteroseismic $\log g$.

surface gravity uncertainties come from the 16- and 84- percentiles of the posterior calculated by BASTA. For $[M/H]$ and ν_I uncertainties, we adapted the method outlined by Epstein et al. (2010).

Summarising their approach, the classical spectroscopic method yields a vector of atmospheric model parameters:

$$\mathbf{m} = (T_{\text{eff}}, \log g, [M/H], \nu_I), \quad (6)$$

which is found when all components of the observables vector \mathbf{o} converge to a zero vector. The components of \mathbf{o} are:

- o_1 : slope of the linear fit from line-by-line Fe I abundances measured against their respective lower excitation potentials;
- o_2 : difference, in dex, between the medians of Fe I and Fe II abundances;
- o_3 : difference, in dex, between $[M/H]_{(\text{Fe}, \alpha)}$ and $[M/H]_{\text{MODEL}}$, and
- o_4 : slope of the linear fit from line-by-line Fe I abundances measured against the logarithm of their respective equivalent widths normalized by their wavelengths.

To propagate the uncertainties from \mathbf{o} to \mathbf{m} , a matrix \mathbf{B} is built making $B_{ij} = \partial o_i / \partial m_j$. The values for B_{ij} adopted here were calculated using the spectral atlas from Arcturus (Hinkle et al. 2000) and are slightly different from those shown in table 2 from Epstein et al. (2010). The propagation of uncertainties is then done by:

$$\sigma^{\mathbf{m}} = \mathbf{B}^{-1} \sigma^{\mathbf{o}} \quad (7)$$

where $\sigma^{\mathbf{m}}$ and $\sigma^{\mathbf{o}}$ are the vectors containing the respective uncertainties of \mathbf{m} and \mathbf{o} . However, the parameters m_1 and m_2 , T_{eff} and $\log g$, respectively, were not calculated by the classical spectroscopic method and thus the values of $\sigma_1^{\mathbf{o}}$ and $\sigma_2^{\mathbf{o}}$ were estimated using the uncertainties for T_{eff} and $\log g$ calculated with the IRFM and BASTA:

$$\sigma_i^{\mathbf{o}} \approx B_{ii} \sigma_i^e \quad (8)$$

where σ_i^e are the uncertainties for T_{eff} and $\log g$ calculated with the other methods.

The value of $\sigma_3^{\mathbf{o}}$ is calculated by perturbing the line-by-line Fe measurements: a vector \mathbf{s} whose size is the number of Fe lines measured in a given star – whose measurements form the vector \mathbf{s}^{Fe} – is sampled from a normal distribution with the star's $A(\text{Fe})$ as mean and the standard deviation of the line-by-line Fe measurements as its scale. Then \mathbf{s}^{Fe} is subtracted from \mathbf{s} and the mean ξ of the components of the resulting vector is calculated. The process is repeated 1000 times, and, finally, $\sigma_3^{\mathbf{o}}$ is taken as the mean of all 1000 ξ values. The value of $\sigma_4^{\mathbf{o}}$ is the uncertainty of the slope of the linear fit used to determine o_4 .

After calculating $\sigma^{\mathbf{m}}$ with Eq. 7, the values of $\sigma_1^{\mathbf{m}}$ and $\sigma_2^{\mathbf{m}}$ are replaced with the uncertainties for T_{eff} and $\log g$ previously calculated. The adopted uncertainties for the atmospheric parameters are shown in Table A1.

The uncertainties for the individual abundances $A(X)$ are estimated by taking the sensitivities of $A(X)$ to 1- σ variation of the atmospheric parameters. Those sensitivities are added in quadrature along with the mean absolute deviation of the line-by-line measurements of the element X , giving the resulting uncertainties $\sigma_{A(X)}$ shown in Table A2.

3.2 Dynamics

The dynamical properties of the stars were determined following the procedure described in Monty et al. (2020). Briefly, we adopted

Table 4. Ages, masses and radii derived with the s_n (T_{eff} , $[M/H]$, $\Delta\nu$, ν_{max} , evolutionary phase, 2MASS K_s) set, as well as adopted $[\text{Fe}/\text{H}]$.

KIC	Age (Gyr)	Mass (M_{\odot})	Radius (R_{\odot})	$[\text{Fe}/\text{H}]$ dex
4345370	$9.2^{+1.1}_{-0.9}$	$0.95^{+0.02}_{-0.03}$	$9.9^{+0.1}_{-0.1}$	-0.75
4671239	$5.4^{+0.4}_{-0.3}$	$1.01^{+0.02}_{-0.02}$	$5.70^{+0.05}_{-0.05}$	-2.63
6279038	$13.8^{+3.4}_{-3.1}$	$0.76^{+0.06}_{-0.05}$	$21.3^{+0.8}_{-0.6}$	-2.11
7191496	$8.7^{+1.6}_{-2.1}$	$0.88^{+0.08}_{-0.04}$	$13.5^{+0.5}_{-0.3}$	-1.92
8017159	$10.1^{+4.7}_{-3.9}$	$0.83^{+0.12}_{-0.09}$	$30.7^{+2.1}_{-1.6}$	-1.52
11563791	$8.8^{+1.5}_{-1.3}$	$0.94^{+0.04}_{-0.04}$	$8.6^{+0.1}_{-0.1}$	-0.78
12017985	$5.5^{+1.3}_{-1.1}$	$1.01^{+0.07}_{-0.06}$	$13.6^{+0.3}_{-0.3}$	-1.89

the potential characterised in McMillan (2017) and implemented in the galactic dynamics Python package, GALPY as McMillan17 (Bovy 2015). The characteristics of the potential components, solar galactocentric distance ($R_0 = 8.21$ kpc), and circular velocity ($v_0 = 233.1$ km/s) given in Table 3 of McMillan were all left unchanged. The solar position was set to $(X, Y, Z) = (0, 0, 20.8)$ pc as given by Bennett & Bovy (2019). We used Gaia EDR3 data for positions, parallaxes (corrected according to Lindegren et al. 2021) and proper motions (Gaia Collaboration et al. 2021). Radial velocities were taken from Gaia DR2 (Gaia Collaboration et al. 2018) for the six objects with radial velocity measurements available in the catalogue. KIC 4671239 does not have radial velocity information in Gaia, thus the value of -187.5 ± 2.0 km s $^{-1}$ for heliocentric radial velocity measured in our observed spectrum was adopted. To explore the errors associated with each dynamical property, we constructed the covariance matrix associated with the Gaia EDR3 parameters for each star. A symmetric error distribution was assumed for the radial velocity values. We performed 1000 MC realisations for each star to sample the error distributions. Stellar orbits were integrated for each realisation, integrating forwards and backwards 5-7 Gyr for a total integration time of 10-14 Gyr.

As in Monty et al. (2020), we recover the actions (J_{ϕ} , J_R , J_z), orbital period (T), eccentricity (e), and maximum height from the galactic plane (Z_{max}) for each star using an implementation of the Stäckel Fudge in GALPY (Binney 2012; Mackereth & Bovy 2018). The three dimensional velocities U , V and W were also determined after accounting for the solar peculiar velocity as determined by Schönrich et al. (2010) (U, V, W) = (11.1, 12.24, 7.25 km/s). Finally, to compare with the inclination values of Yuan et al. (2020), we estimate the orbital inclination as the orbit-averaged angle between the total angular momentum $|L_{\text{tot}}|$ and the z -component of the angular momentum L_z .

4 AGES FROM GRID-BASED MODELLING

As explained in the Section 3, in this work we tested two sets of observables, one – s_p – that does include parallaxes and a second one – s_n – that does not. In s_p we have made three runs using Gaia parallaxes: (a) employing values published by Gaia DR2 (Gaia Collaboration et al. 2018) and corrected according to Zinn et al. (2019a); (b) using parallaxes from Gaia EDR3 (Gaia Collaboration et al. 2021) and corrections from Lindegren et al. (2021); and, finally, (c) also using EDR3 parallaxes, but this time increasing the published uncertainties by 0.02 mas (in order to decrease the weight of parallax in the solution). The effect of these changes can be seen in Fig. 3, where the ages of these three different s_p runs are plotted as function of s_n ages.

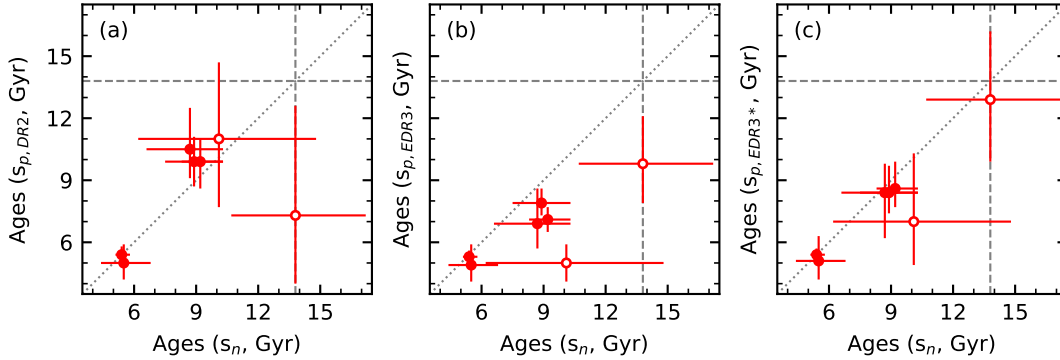


Figure 3. Comparison between ages derived with s_n (T_{eff} , $[M/H]$, $\Delta\nu$, ν_{max} , evolutionary phase, 2MASS K_s) and ages calculated with s_p (i.e., s_n plus parallax) using different parallax inputs from Gaia. (a): s_p adopts DR2 parallaxes; (b): s_p adopts EDR3 parallaxes; (c): same as (b), but inflating the parallax uncertainties by 0.02 mas. Dashed lines represent the age of the Universe (Planck Collaboration et al. 2020), while dotted lines show the identity function. Filled circles have asteroseismic parameters compiled from Yu et al. (2018), while open circles represent stars with parameters from Pinsonneault et al. (2018).

Fig. 3(a) shows agreement between s_p and the pure asteroseismic solution s_n within the error bars, except for KIC 6279038 – the oldest star in the s_n set. The overall agreement between s_n and s_p seen in Fig. 3(a) is expected since the parallax corrections employed in this s_p set have been calibrated with asteroseismology (Zinn et al. 2019a).

When Gaia EDR3 parallaxes are employed, as shown in Fig. 3(b), s_p error bars decrease, but the 1- σ agreement disappears for several stars. In particular, KIC 8017159 – the second-oldest in the s_n set – now displays a very small uncertainty in s_p age, but with the median age now being similar to the youngest s_n object at ~ 5 Gyr. Also, using parallaxes now yields lower ages to all targets, while the opposite happens to most of our stars when DR2 parallaxes are employed.

In order to check if the results found with Gaia EDR3 parallaxes might be affected by some systematics we did another s_p run with EDR3 error bars increased by 0.02 mas – making them slightly larger than those from DR2, whose results are shown in Fig. 3(c). With the slightly larger error bars resulting from the increase in the uncertainty of the parallax, the relationship between s_p and s_n is closer to 1:1, including for KIC 6279038. However, KIC 8017159 keeps being younger, albeit with the error bar now touching the identity function. The overall result suggests that Gaia EDR3 parallax uncertainties might be underestimated if the pure seismic solutions are reliable, and employing them without any corrections might result in trading accuracy for precision in several cases, at least in the lower ($M \lesssim 1.0 M_{\odot}$) mass regime. These results converge to agreement with findings both from the Gaia team and independent studies that the published parallax uncertainties from Gaia EDR3 might be underestimated at least for some regions of the parameter space (El-Badry et al. 2021; Fabricius et al. 2021; Zinn 2021).

Regarding KIC 8017159, the DR2-EDR3 parallax difference is 0.05 mas while the uncertainty in EDR3 is $\sigma_{\varpi} \approx 0.01$ mas, i.e., the difference is of the order of 5- σ . Its EDR3 RUWE is 0.88, while other astrometric quality flags suggested by Fabricius et al. (2021) such as `ipd_harmonic_amplitude`, `ipd_multi_peak`, `phot_bp_rp_excess_factor`, and the excess noise of the source `astrometric_excess_noise` also display good values, thus the astrometric solution is expected to be good.

However, other program stars have had even larger variations between DR2 and EDR3 parallaxes, as seen in Table 1, but their GBM solutions were not as sensitive to parallax as in the case of

KIC 8017159. According to the results from our GBM, this object and KIC 6279038 are upper-RGB stars – i.e. RGB stars whose ν_{max} is lower than $10 \mu\text{Hz}$. The result for the evolutionary stage is always RGB for all stars in this work regardless of the chosen prior (RGB or none). As shown in Fig. 3, these objects on the upper-RGB also have the worst precision in the modelled ages, regardless of the chosen input set. Zinn et al. (2019b) have found a departure from the scaling relation for stellar radii on the upper-RGB, suggesting that we might not understand very well the relationship between stellar pulsations and fundamental parameters in this region of the HR diagram. However, it must be noted that this departure has been identified for radii $> 30 R_{\odot}$, while our program stars have $R \lesssim 30 R_{\odot}$.

Given the large change in Gaia parallaxes from DR2 to EDR3 in some of our stars and the resulting differences in modelled ages that have arisen from that, adopting the ages derived from the pure seismic solution (s_n) seems to be the safest option in this study. The choice of one set over the other has negligible impact on the atmospheric parameters used in the spectroscopic analysis – the change in $\log g$ is of the order of 0.01 dex, and the resulting impact on abundances is negligible. Nevertheless, the ages estimated for stars on the upper RGB must be interpreted with caution.

In order to do a sanity check, we also compare the results derived with the s_n input set with results taken from PARAM (da Silva et al. 2006; Rodrigues et al. 2014)⁵, using the same observational inputs and this time employing the models from Rodrigues et al. (2017). Modelling with PARAM yields larger stellar masses for three objects, although both PARAM and BASTA error bars overlap the identity function with the exception of KIC 11563791, whose PARAM age is $7.0^{+1.1}_{-0.9}$ Gyr and PARAM mass is $0.98^{+0.04}_{-0.03} M_{\odot}$. These slightly larger masses correspond to (slightly) lower ages derived by PARAM. One notable object in this comparison is KIC 6279038, which shows a negligible difference in stellar mass and an 1 Gyr difference in (median) age.

In their study of asteroseismology of eclipsing binaries, Brogaard et al. (2018) noted that the models from Rodrigues et al. (2017) are possibly too cool in T_{eff} . This could lead to overestimation of stellar mass for a given observed T_{eff} value. The difference in the masses

⁵ Using the web form available at <http://stev.oapd.inaf.it/cgi-bin/param>.

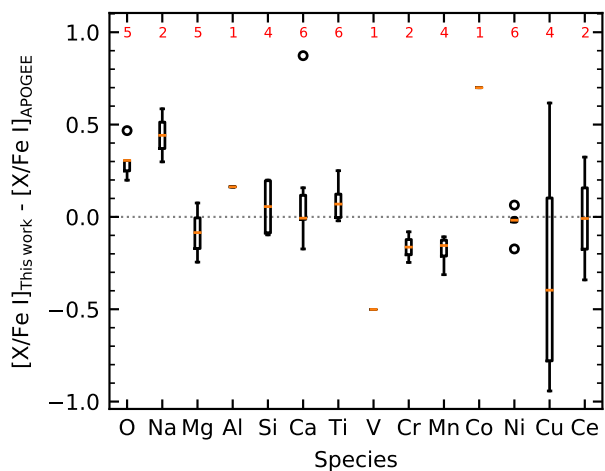


Figure 4. Boxplot showing the abundance ratio differences for each species between this work and APOGEE (Jönsson et al. 2020). Boxes represent the interquartile ranges (IQR), orange lines are the medians, whiskers correspond to $1.5 \times \text{IQR}$, and circles are outliers. Red figures on top show the number of data points for each species (i.e., stars that have measurements in both works).

derived for KIC 11563791 corresponds to a T_{eff} shift of -100 K in the scaling relations, assuming the same $f_{\Delta\nu}$ in the shifted and non-shifted cases. Another possible source of the (small) disagreement seen between BASTA and PARAM are differences in each approach of GBM (see, e.g., Serenelli et al. 2017, for a comprehensive discussion).

In Section 3 it is mentioned that the adopted mass loss prescription is $\eta = 0.3$. All stars in this study are still ascending the RGB, thus we expect negligible effects because their radii are $\lesssim 30 R_{\odot}$. In order to check the effect of different choices of the mass loss parameter we also performed a s_n run, this time using $\eta = 0$. Intuitively, the exclusion of mass loss should result in older ages, because the current asteroseismic mass is supposed to be the same in both cases, i.e., in the $\eta = 0$ scenario the initial mass would be lower. This is observed for core He-burning stars, but not on the RGB, where there is no clear conclusion (see Casagrande et al. 2016). When isochrones with and without mass loss are plotted against each other in a Kiel diagram, the model with $\eta = 0$ is slightly cooler in the upper RGB. Thus, for a fixed set of observables, the $\eta = 0$ scenario would require a younger isochrone (relative to $\eta = 0.3$) to fit the input parameters. However, the difference between the isochrones in this evolutionary stage ($1.3 < \log g < 2.0$) is small enough that the random uncertainties in the input observables likely dominate over different choices of mass loss prescription. Indeed, in our $\eta = 0$ test, no clear systematic shift has been found in stellar ages, nor large ($\geq 1\text{-}\sigma$) deviations in the median ages have been detected.

5 RESULTS AND DISCUSSION

As briefly discussed in Section 1, information from spectra, astrometry, and stellar oscillations allow an in-depth characterisation of individual stars. In this Section we will both revisit the discussion on the age-chemistry-kinematics relationships of the objects in common with Epstein et al. (2014) and those picked from Casagrande et al. (2014).

Six of the seven stars in this study have results from APOGEE

(Jönsson et al. 2020). In Fig. 4 we compare our abundance ratio results for the species with measurements in common with their work. This time we normalise the abundances by Fe I to make the comparison with APOGEE consistent. Among the $[X/\text{Fe}]$ ratios with at least two measurements compared, $[\text{O}/\text{Fe}]$ and $[\text{Na}/\text{Fe}]$ have larger values in this study, while the $[\text{Cu}/\text{Fe}]$ difference among both works has a very large scatter. The outlier in $[\text{Ca}/\text{Fe}]$ corresponds to KIC 12017985, whose $[\text{Ca}/\text{Fe}]$ in APOGEE is -0.61 dex. The median differences⁶ in T_{eff} , $\log g$, and $[\text{Fe I}/\text{H}]$ are 27 K, -0.038 dex, and 0.10 dex, respectively. The median absolute deviations for differences in these parameters are, respectively, 43 K, 0.028 dex, and 0.11 dex. When taking into account the uncertainties from this work and the typical ones from APOGEE (~ 100 K in T_{eff} , 0.1 dex in $\log g$, and 0.02 dex in $[\text{Fe I}/\text{H}]$), the differences in atmospheric parameters are negligible. This also suggests a good accuracy in the seismic-calibrated spectroscopic $\log g$ calculations from Jönsson et al. (2020).

5.1 Revisiting the metal-poor stars from APOKASC

Five of the metal-poor objects from APOKASC studied by Epstein et al. (2014) were also analysed in this work, and here we adopt the same identification as in their work for these targets (see Table 1). From our GBM all five are metal-poor stars on the RGB, and three of them (KIC 7191496, KIC 8017159 and KIC 11563791) have retrograde orbits. KIC 4345370 was classified by Epstein et al. as belonging to the thick disc – its orbit is the least eccentric in this subset although it shows some moderate departure from the disc plane ($|Z_{\text{max}}| \approx 2.8$ kpc). The modelling of KIC 12017985 shows a prograde albeit highly eccentric and inclined orbit ($|Z_{\text{max}}| \approx 4$ kpc). However, the results for KIC 12017985 must be interpreted with caution due to its large RUWE value published in Gaia EDR3.

Epstein et al. (2014) highlighted a few possibilities to explain the discrepancy between their expected mass values for the metal-poor halo stars and their measurements. The authors suggested that a metallicity-based correction would be needed in the scaling relations in order to calculate accurate stellar parameters. Indeed, as shown in Fig. 5, mass estimations using model-based corrections resulted in lower masses, both in this work and in the literature. Overall, the corrected masses are in or close to the range that Epstein et al. have expected for halo stars, the exceptions in this work being KIC 11563791, whose error bar is $\sim 0.03 M_{\odot}$ above the estimated value in fig. 2 from Epstein et al., and KIC 12017985.

The ages derived with the s_n input set have their error bars for KIC 7191496 and KIC 11563791 (A and D) barely touching the 10 Gyr mark defined as the lower limit for the halo by Epstein et al. Nonetheless, if we consider the older ages derived with the s_p (DR2) input set (see Fig. 3(a)), their values for KIC 7191496 and KIC 11563791 are more compatible with halo expectations. However, when EDR3 parallaxes are employed the result is qualitatively the same as that obtained with s_n – i.e., they are younger than the 10-Gyr limit. Meanwhile, the result for KIC 4345370 (H) is consistent with the age for the thick disc (8-13.77 Gyr). The large error bars for KIC 8017159 (C) in Fig. 5 might be explained by some difficulty to extract the average seismic parameters is its case, as already discussed by Epstein et al. The fractional $\Delta\nu$ uncertainty adopted here is $\sim 2\%$, while for all the other four targets in this subset the fractional uncertainties for the same observable are below 1%. Also, being on the edge of the parameter space might result in loss of accuracy, as the $0.05 \mu\text{Hz}$ difference in $\Delta\nu$ between Epstein et al. and the

⁶ This work values minus APOGEE values.

Table 5. Abundance ratios [X/Fe], A(Li), and [Fe/H].

KIC	A(Li)	[O/Fe]	[Na/Fe]	[Mg/Fe]	[Al/Fe]	[Si/Fe]	[Ca/Fe]	[Sc/Fe]	[Ti/Fe]
4345370	0.92 ± 0.12	0.47 ± 0.07	0.02 ± 0.10	0.22 ± 0.08	0.21 ± 0.08	0.27 ± 0.06	0.05 ± 0.10	0.10 ± 0.07	0.02 ± 0.08
4671239	0.11 ± 0.18	0.14 ± 0.17	...	0.29 ± 0.20
6279038	...	1.11 ± 0.15	...	0.45 ± 0.14	0.52 ± 0.14	0.14 ± 0.15	0.43 ± 0.17
7191496	0.15 ± 0.15	0.15 ± 0.11	0.39 ± 0.17
8017159	...	0.50 ± 0.12	...	0.02 ± 0.11	...	0.08 ± 0.12	0.14 ± 0.15	-0.06 ± 0.11	-0.14 ± 0.23
11563791	...	0.50 ± 0.13	-0.29 ± 0.13	0.08 ± 0.13	...	0.26 ± 0.13	0.05 ± 0.13	-0.07 ± 0.13	-0.12 ± 0.15
12017985	1.23 ± 0.13	0.94 ± 0.15	-0.07 ± 0.15	0.36 ± 0.15	...	0.24 ± 0.16	0.36 ± 0.15	0.07 ± 0.15	0.41 ± 0.16
KIC	[V/Fe]	[Cr/Fe]	[Mn/Fe]	[FeI/H]	[FeII/H]	[Co/Fe]	[Ni/Fe]	[Cu/Fe]	[Zn/Fe]
4345370	-0.24 ± 0.11	-0.28 ± 0.07	-0.64 ± 0.09	-0.89 ± 0.11	-0.75 ± 0.07	-0.10 ± 0.07	-0.06 ± 0.12	0.06 ± 0.08	0.71 ± 0.07
4671239	-2.63 ± 0.20
6279038	0.06 ± 0.15	...	-0.34 ± 0.15	-1.94 ± 0.17	-2.11 ± 0.16	...	0.15 ± 0.14	-0.38 ± 0.16	0.20 ± 0.14
7191496	-1.98 ± 0.21	-1.92 ± 0.12	...	0.07 ± 0.12	...	0.10 ± 0.10
8017159	-0.32 ± 0.12	-1.56 ± 0.18	-1.52 ± 0.13	...	-0.24 ± 0.11	...	-0.03 ± 0.12
11563791	-0.29 ± 0.13	-0.34 ± 0.13	-0.82 ± 0.13	-1.03 ± 0.12	-0.78 ± 0.15	...	-0.26 ± 0.14	-0.36 ± 0.13	0.66 ± 0.19
12017985	0.07 ± 0.17	...	-0.32 ± 0.15	-1.79 ± 0.17	-1.89 ± 0.17	...	0.15 ± 0.15	-0.35 ± 0.15	0.18 ± 0.15
KIC	[Sr/Fe]	[Y/Fe]	[Zr/Fe]	[Ba/Fe]	[La/Fe]	[Ce/Fe]	[Nd/Fe]	[Sm/Fe]	[Eu/Fe]
4345370	0.25 ± 0.10	-0.06 ± 0.15	-0.08 ± 0.14	0.14 ± 0.12	0.14 ± 0.08	0.19 ± 0.15	0.35 ± 0.18	0.31 ± 0.06	0.04 ± 0.06
4671239
6279038	...	-0.04 ± 0.14	...	0.07 ± 0.14	0.43 ± 0.14	0.25 ± 0.15	0.54 ± 0.14	0.62 ± 0.15	...
7191496	...	0.06 ± 0.11	...	-0.23 ± 0.10
8017159	...	-0.21 ± 0.11	-0.11 ± 0.13	-0.07 ± 0.12	-0.13 ± 0.11	...	0.21 ± 0.11
11563791	...	0.44 ± 0.13	...	0.33 ± 0.15	0.28 ± 0.13	...	0.20 ± 0.13	0.67 ± 0.14	-0.15 ± 0.13
12017985	...	0.08 ± 0.15	...	-0.07 ± 0.15	0.43 ± 0.15	0.34 ± 0.15	0.50 ± 0.15	...	0.14 ± 0.16

APOKASC-2 value adopted in this work propagates to a 34 % shift in stellar mass in the scaling relations. A comprehensive discussion on the precision and accuracy of $\Delta\nu$ and ν_{\max} measurements can be found, e.g., in section 3 of [Yu et al. \(2018\)](#). The ages derived in this work for this subset of targets seem to be in an intermediary position between those published by APOKASC-2 and those expected for a halo population – the exception being KIC 12017985 (B), whose ages agree in both datasets. For KIC 8017159, the age uncertainties are larger than those published by APOKASC-2 despite similar error bar sizes in mass.

In order to investigate potential systematics arising from different choices of scaling relation inputs, Fig. 5 also compares masses derived using pure scaling relations (mass_{PSR}), i.e., without any correction factors. For instance, KIC 12017985 has mass_{PSR} larger than the uncorrected mass published by [Yu et al.](#) due only to the larger T_{eff} adopted in this work, because the average seismic parameters are the same in both studies. Also, it can be seen that the larger uncertainties in both $\Delta\nu$, ν_{\max} and T_{eff} in [Epstein et al.](#) result in much larger error bars in mass_{PSR} . The larger corrected mass of KIC 7191496 in [Yu et al.](#) might be a result of a different choice of correction factor, while the larger KIC 11563791 mass in their results might also be a combination of T_{eff} and correction factor choices. A similar point about these differences has been made by [Valentini et al. \(2019\)](#), whose results are also shown in Fig. 5.

The cyan points in Fig. 5 show our results if we adopt the values from [Epstein et al.](#) for our s_n input. As expected from what is shown in the mass_{PSR} plot in Fig. 5, the error bars become so large that it is impossible to make any claim about halo membership from these ages. The results from [Valentini et al. \(2019\)](#) are compared as well. They show larger error bars similar to those from our re-analysis of [Epstein et al.](#), possibly linked to their larger input uncertainties. Although both results are compatible with those from the s_n set, the difference in the error bars hint at the required level of precision in the

input parameters for age estimation. Also, it is important to note that the reanalysis of [Epstein et al.](#) has differences between some inputs and fitted parameters for all targets in GBM. Most notably T_{eff} , whose fitted values differ from the inputs by more than $1-\sigma$ in all five stars, even with input T_{eff} possessing relatively large uncertainties (125–176 K). The fitted temperatures are always hotter than the inputs. Differences between the results from [Sharma et al. \(2016\)](#) and our reworked analysis of [Epstein et al. \(2014\)](#), cyan circles in Fig. 5 are likely the result of different choices of corrections for the scaling relations.

The bottom plot in Fig. 5 shows the different values of metallicity adopted. Although not present in the pure scaling relations, the metallicity plays a role in model-dependent calculations of the stellar parameters – correction factors and stellar model fitting. Our [M/H] values are systematically higher than those estimated by [Valentini et al. \(2019\)](#), although within the error bars. Nevertheless, the effect of different [M/H] choices seems to be mild. For instance, adopting [Valentini et al.](#) or [Epstein et al.](#) [M/H] values would increase the mass of KIC 7191496 by 0.02 or 0.04 M_{\odot} , respectively, without affecting the resulting uncertainties. The resulting age would be qualitatively the same, with differences from our adopted value staying below $1-\sigma$.

5.1.1 KIC 12017985

The age of $5.5^{+1.3}_{-1.1}$ Gyr, estimated for KIC 12017985, seems too young for Halo membership, being closer to what is expected for the thin disc. However, assuming that its Gaia EDR3 astrometric solution can be trusted for modelling its kinematics, the dynamical characteristics of KIC 12017985 are not expected for a thin disc star (e.g., relatively low L_z and large eccentricity). Our reanalysis of the [Epstein et al. \(2014\)](#) data and the results from [Valentini et al. \(2019\)](#) give older ages, but their associated uncertainties are too

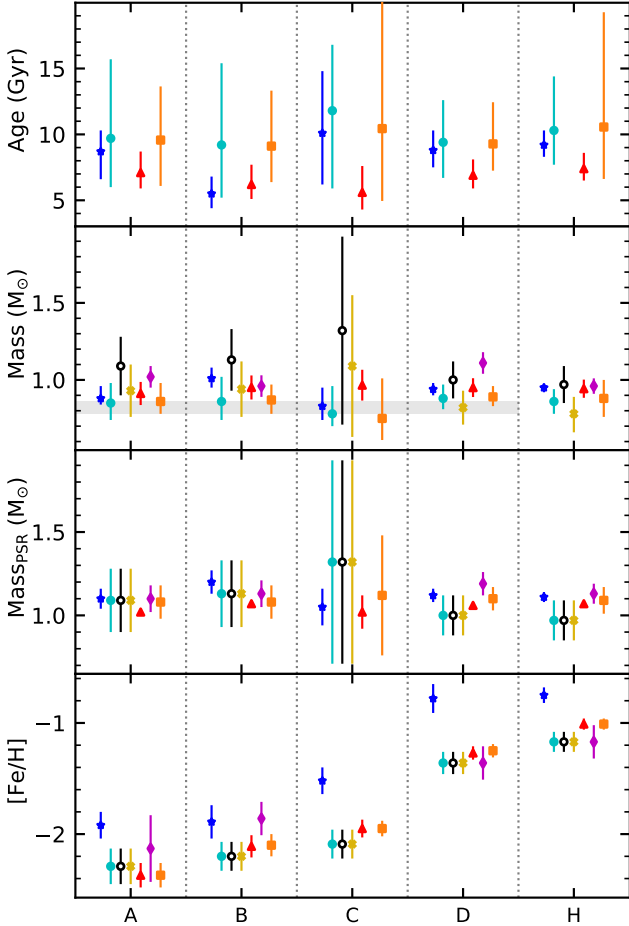


Figure 5. Comparison with values in selected works from the literature for the stars in common with Epstein et al. (2014). See Table 1 for the corresponding KIC IDs. From top to bottom: ages, published masses, masses from *pure scaling relations* given by the published values of $\Delta\nu$, ν_{\max} and T_{eff} in each paper, and $[\text{Fe}/\text{H}]$. Blue stars: this work (s_n). Cyan circles: grid-based modelling using the s_n input set (T_{eff} , $[\text{M}/\text{H}]$, $\Delta\nu$, ν_{\max} , evolutionary phase, 2MASS K_s) with $\Delta\nu$, ν_{\max} and T_{eff} published by Epstein et al.. Black open circles: values published in Epstein et al.. Golden crosses: Sharma et al. (2016, fig. 12). Red triangles: APOKASC-2 (Pinsonneault et al. 2018). Magenta diamonds: values from Yu et al. (2018). Orange squares: Valentini et al. (2019). The grey shaded area represents the $2\text{-}\sigma$ mass range expected by Epstein et al..

large and reach values compatible with both thin disc and the age of the Universe. From the chemical point of view, KIC 12017985 abundances are compatible with those expected from an old halo population – e.g., $[\text{Mg}/\text{Fe}] = [\text{Ca}/\text{Fe}] = 0.36$ dex, and it has high Ti I and O abundances as well. Some of its s-process elements abundances are relatively high (e.g., La, Ce and Nd). KIC 12017985 has detection of Li; $A(\text{Li})_{\text{LTE}} = 1.23$ dex.

Bandyopadhyay et al. (2020) made a high-resolution chemical analysis of KIC 12017985 and their abundance ratios are systematically lower than ours with very few exceptions (Ni and Ba). The differences are probably due to different sets of atmospheric parameters adopted - their classical spectroscopic analysis gave values closer to our initial spectroscopic guesses for the atmospheric parameters, however our adopted IRFM T_{eff} is 275 K hotter than the Bandy-

opadhyay et al. value and our seismic $\log g$ is ~ 0.7 dex larger. If our adopted T_{eff} and metallicity values are replaced by the purely spectroscopic ones, BASTA is not able to find a solution, as it pushes the results towards the boundary of the parameter space (age ≈ 19 Gyr). Also, no agreement is found between input and output T_{eff} , $\Delta\nu$ and ν_{\max} when the spectroscopic parameters are employed.

Belokurov et al. (2020) argue, using Gaia DR2 data, that large RUWE values are related to binarity. If KIC 12017985 (RUWE = 2.8 in Gaia EDR3) is a member of a multiple system, its relatively large mass could be explained by past mass accretion from a companion that it is masking the age if this red giant, i.e., KIC 12017985 would be a blue straggler. The results found to date for this object make it a good target for a long-term campaign of radial velocity monitoring in order to check if it is a member of a binary system. Another possibility is KIC 12017985 being a member of some uncatalogued dwarf galaxy recently accreted by the Milky Way.

5.1.2 KIC 4345370 and KIC 11563791

KIC 11563791 and KIC 4345370 display similar metallicities ($[\text{Fe}/\text{H}] \sim -0.75$). However, while the later is a member of the thick disc, the former has a retrograde orbit. KIC 11563791 is more metal-rich than the other stars with retrograde orbits in this study, and it presents a relatively peculiar composition. It presents near-solar Mg and Ca, while at the same time it is Si- and O-rich (see Table 5). It is also an outlier in Y, with $[\text{Y}/\text{Fe}] = 0.44$, and it has low $[\text{Eu}/\text{Fe}]$ relative to objects of similar metallicity in this work.

Among the stars with Zn measurements, KIC 11563791 and KIC 4345370 display strong enhancement in this species, around +0.7 dex as shown in Table 5. They also display (relative) depletion in Cr and Mn, which could hint at an Hypernova-dominated origin of their primordial gas (Nomoto et al. 2013). However, the Hypernova scenario would be challenged by their observed V and Co abundances, as both elements are expected to be enriched together with Zn on sites with very large explosion energies. Another caveat is the fact that such a scenario is predicted in a more metal-poor regime, as also discussed by Nomoto et al.. Given their ages (~ 9 Gyr), Zn production in the Universe is thought to be dominated by core-collapse supernovae at the chronological point of their formation. However, this pair of stars also display mild enhancement in Ba and La abundances (see Table 5), and their $[\text{Ba}/\text{Fe}]$ abundances suggest enrichment mostly by the s-process (Kobayashi et al. 2020).

5.2 KIC 4671239 and KIC 6279038

KIC 4671239 and KIC 6279038 are metal-poor objects identified by the SAGA Survey (Casagrande et al. 2014). The $\Delta\nu$ values published by Casagrande et al. and APOKASC-2 for KIC 6279038 are larger than the $\Delta\nu$ published by Yu et al. by $0.136 \mu\text{Hz}$, or $3\text{-}\sigma$. The difference in ν_{\max} is not as large, being lower than $1\text{-}\sigma$. Such difference is expected to have a significant impact in age estimation, although not in $\log g$.

In order to evaluate the impact of the $3\text{-}\sigma$ $\Delta\nu$ deviation in age estimations, new s_n runs were made employing the observables published by Yu et al. and APOKASC-2. The resulting distributions are shown in the violin plots in Fig. 6. It is evident from inspection that the increased value of $\Delta\nu$ – adopted in this work – yields a much larger age. It must be pointed out that the disparity between different sets of input values taken from the literature is large enough to characterise this metal-poor object as either young or old – despite the considerable uncertainties in the ‘young’ case. Visual inspection

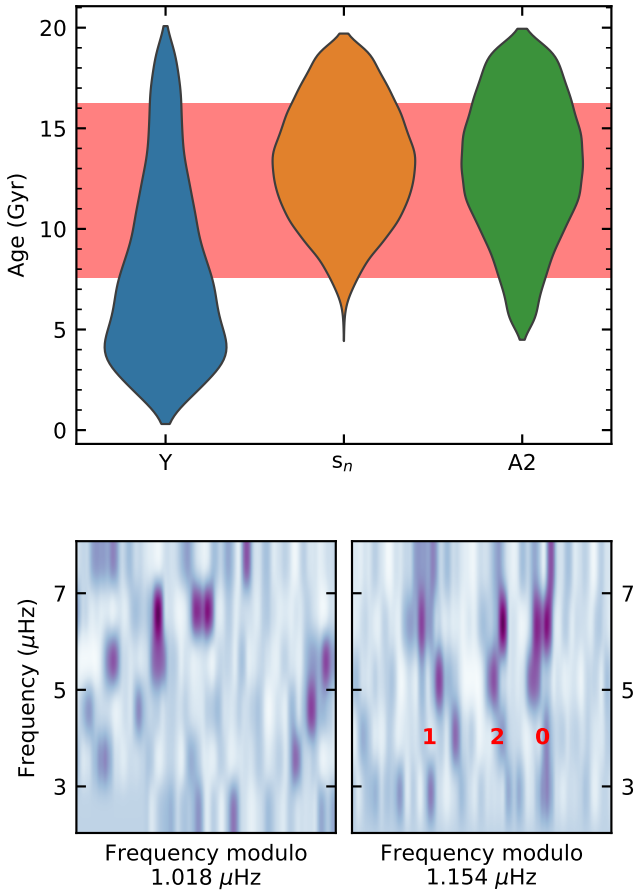


Figure 6. *Top:* Violin plots illustrating the age distributions for KIC 6279038 resulting from different values of input parameters – T_{eff} , $[M/H]$, $\Delta\nu$, and ν_{max} . *Left:* using $\Delta\nu$ and ν_{max} from Yu et al. (2018) (Y), and T_{eff} and $[M/H]$ calculated in this work; *centre:* from the values shown in Tables 1 and 3; *right:* using input parameters published by Pinsonneault et al. (2018, APOKASC-2) (A2). The shaded area shows the $1-\sigma$ age interval given in the APOKASC-2 catalogue. *Bottom:* echelle plots folded by $\Delta\nu$ values published in APOKASC-2 (right) and Yu et al. (left). Numbers in the right plot indicate the angular degrees l .

of the echelle plots created with the corresponding $\Delta\nu$ values as frequency modulo indicate that the value published in APOKASC-2 is more accurate than that from Yu et al.. The ridges expected to be seen in the echelle plots of solar-like oscillators are more apparent in the former. Also, the mode structure seen in the (correct) echelle plot in Fig. 6 agrees with the expected (and observed) behaviour for luminous stars, with the dipole modes being further away from the $l=0,2$ pair at higher frequencies (Stello et al. 2014, figs. 1 and 3).

The disagreement between the results for KIC 6279038 illustrates the shortcomings of the characterization of low $\log g$ stars using Kepler data. Its Gaia parallax gives no improvement to the estimation, because it is the most distant star in this work and parallaxes from both data releases are similar – $\varpi_{\text{DR2}} = 0.1928 \pm 0.0271$ mas after employing the zero-point correction from Zinn et al. (2019a), while (corrected) $\varpi_{\text{EDR3}} = 0.1898 \pm 0.0099$ mas (Gaia Collaboration et al. 2021; Lindegren et al. 2021).

KIC 4671239 is a lower RGB ($\log g \sim 3$) object and the most

metal-poor target studied in this work. Few species were measured due to low S/N in the observed spectrum. However, it is an interesting object as its $[Mg/Fe]$ and $[Ca/Fe]$ are slightly above 0.1 dex – although it shows enhancement in Ti – while being a relatively massive and metal-poor object, with $1.01 \pm 0.02 M_{\odot}$ and $[Fe/H] = -2.63 \pm 0.20$. It has a very elongated polar orbit according to our modelling ($J_{\phi}/J_{\text{tot}} \approx 0.3$; $R_{\text{peri}} = 1.0$ kpc; eccentricity = 0.79), and, kinematically, it seems to belong to the heated thick disc (Koppelman et al. 2018; Helmi 2020).

The mass/age of KIC 4671239 is too large/young when compared with expectations for a metal-poor halo star. The simplest explanation is the possibility of this object being a blue straggler, as suspected for KIC 12017985. However, at least from its Gaia EDR3 astrometry, there is no evidence of binarity. On the other hand, KIC 4671239 seems to have a peculiar photometry: a spectral energy distribution fitting with VOSA (Bayo et al. 2008) using the atmospheric parameters from Table 3 reveals some flux excess on the WISE W3 region ($\sim 12 \mu\text{m}$, Cutri et al. 2014). Unfortunately, its W4 magnitude only has an upper limit published (quality flag ‘U’), but it can be speculated that KIC 4671239 did suffer a merger in the past, and this infrared excess would be the observational evidence of a debris disc resulting from such event. The same argument has been made by Yong et al. (2016) to suggest that a few young α -rich stars displaying infrared excess in their photometry would indeed be blue stragglers, and it can explain why the asteroseismic mass of this red giant is too large when its low metallicity is taken into account in the context of Galactic chemical evolution. The presence of two out of seven blue stragglers in our sample of metal-poor red giants would not be a surprise given that around one fifth of nearby halo stars are thought to be blue stragglers (Casagrande 2020).

5.3 Accreted stars?

Given the intriguing results in stellar ages derived from asteroseismology for the sample analysed in this work – mostly still younger than usually expected for halo stars, it might be insightful to check their chemodynamics. As noted by Koppelman et al. (2019), the highly retrograde overdensity originally called Gaia-Sequoia (Barbá et al. 2019; Myeong et al. 2019) can be separated in two distinct groups in the energy-angular momentum space – high- and low-energy groups. The former would be *Sequoia proper* while the later was called *Thamnos* by Koppelman et al.. In Fig. 7(c) their separation is located at $E/E_{\odot} \sim 1$.

Monty et al. (2020), in their study of accreted populations, suggested that the α -knee (the location at which the $[\alpha/Fe]$ ratio begins to drop) of Gaia-Sequoia *high orbital energy* starts at $[Fe/H] \approx -2.2$. Their results are reproduced in Fig. 8, as well as in Fig. 7(a,c,d). When α -element composition is taken into account one can spot certain agreement between KIC 8017159 ($[Fe/H] = -1.52$) and the Gaia-Sequoia α -knee fits in $[Mg,Ca/Fe]$. The low-energy group (i.e., Thamnos, purple circles in Fig. 8) seems to have its α -knee located at a higher metallicity with respect to the high-energy group. Looking at Fig. 7(c), KIC 8017159 (C) falls in the valley that seems to divide both groups (Sequoia and Thamnos), sharing the same region of the Energy-Momentum space as well as similar orbital parameters with the globular cluster FSR 1758 (Myeong et al. 2019). If we consider the group of stars identified with the Gaia-Sausage event by Yuan et al. (2020), which overlaps with Gaia-Sequoia in Fig. 7(a,b) it could be argued that KIC 8017159 belongs to Gaia-Sausage instead of Gaia-Sequoia/Thamnos. On the other hand, if we apply constraints similar to those adopted by Feuillet et al. (2020) and Limberg et al. (2021) to the Gaia-Sausage event (eccentricity ≥ 0.8 ; $-600 \leq J_{\phi} \leq$

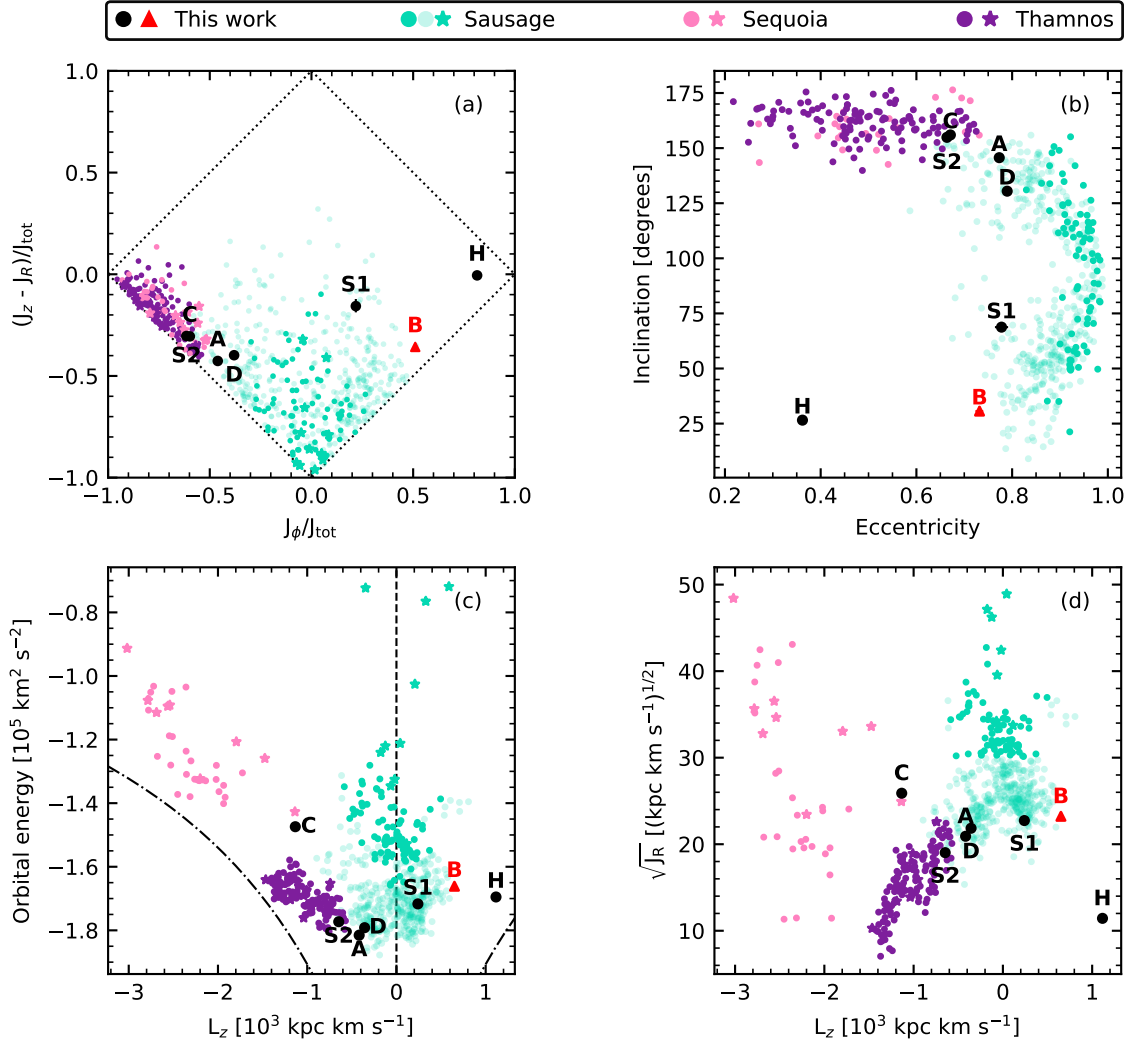


Figure 7. Dynamical parameter space evaluated in this work. Black circles represent the stars in this study other than KIC 12017985 (B) (Gaia EDR3 RUWE = 2.8), marked as a red triangle. See Table 1 for the corresponding KIC IDs. Error bars not shown are smaller than their respective markers. Star markers are data from Monty et al. (2020). Points are from Yuan et al. (2020). Turquoise colour corresponds to Gaia-Sausage, pink refers to Gaia-Sequoia, purple represents low-energy retrograde stars corresponding to Thamnos (i.e., Sequoia G1 from Monty et al.; DTGs 21, 24 and 29 from Yuan et al.). Light turquoise markers represent stars identified as Gaia-Sausage by Yuan et al. that do not pass more strict constraints seen in the literature (see text). (a) Action space. (b) Orbital inclination as function of eccentricity. (c) Orbital energy vs. z -component of angular momentum L_z . The black dashed line ($L_z = 0$) corresponds to a non-rotating orbit. The dash-dotted lines show circular (prograde and retrograde) orbits. (d) Square root of the radial action J_R as function of L_z .

+500 kpc km s^{-1} ; $900 \leq J_R \leq 2500 \text{ kpc km s}^{-1}$), KIC 8017159 clearly does not belong to it. Its non-membership of Gaia-Sausage seems clear when we take into consideration the radial action in Fig. 7(d).

Meanwhile, it can be suggested that KIC 6279038 (S2) belongs to Thamnos. Its metallicity places it between both Sequoia and Sausage α -knees, and combining its α -enhancement and position in the Energy-Momentum space makes it a typical member of Thamnos. If Sequoia and Thamnos belong to the same accreted satellite, KIC 6279038 would be an older, more metal-poor member, while KIC 8017159 would represent a younger, less metal-poor member that formed just before the accretion. However, if the more broad dynamical definition of Yuan et al. is considered, it could either be a member of Thamnos or Gaia-Sausage (see Fig. 7), as both groups are not separable by chemical composition in Fig. 8.

From Fig. 7, KIC 7191496 and KIC 11563791 (A and D) seem

to lie near the transition zone between Gaia-Sausage and Thamnos. They might be members of the former if the Yuan et al. definition is considered. However, KIC 7191496 has $[\text{Ca}/\text{Fe}]$ more compatible with Gaia-Sequoia, putting it in the low- α sequence in Fig. 8.

Regarding KIC 11563791, it is more metal-rich than the other objects in this study with retrograde orbits, and its chemical composition is similar to KIC 4345370, a thick disc member. The lower $[\text{Mg}/\text{Fe}]$ of the former with respect to the later may hint on an *ex-situ* origin (Di Matteo et al. 2019). Also, the $[\text{Ni}/\text{Fe}]$ in KIC 11563791 is 0.2 dex lower than in KIC 4345370, further suggesting an accreted origin, as objects formed in satellites tend to be deficient in this element (Montalbán et al. 2021). However, the Ni abundance in KIC 7191496 is solar, and its $[\text{Ca}/\text{Fe}]$ seems too low in comparison with the trend from Gaia-Sausage in Fig. 8, as mentioned in the previous paragraph. In this case, KIC 7191496 and KIC 11563791 would be unrelated in Galactic history despite showing very similar

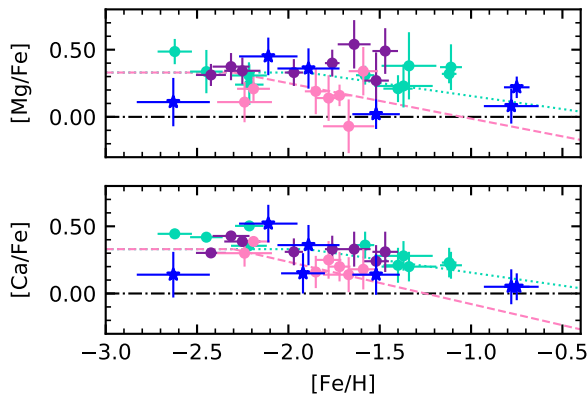


Figure 8. [Mg,Ca/Fe] plots showing Gaia-Sequoia and Gaia-Sausage α -knee fits according to Monty et al. (2020, pink and turquoise lines, respectively). Blue stars: this work. From Monty et al. – Pink and purple circles: Gaia-Sequoia high ($E/E_{\odot} < 1$) and low orbital energy samples, respectively. Turquoise circles: Gaia-Sausage.

ages and dynamics. Such result is not unexpected, as over-densities of multiple accretion events may overlap between each other and with the *in-situ* population (Jean-Baptiste et al. 2017). Given that the degeneracy among accretion events expected in dynamical space is broken only partially with the use of two out of three observational sources of information (chemistry, kinematics, chronology), precise red giant ages derived from solar-like oscillations for a large number of halo stars, as done in this work for a small dataset, may be useful to further characterise different events (if separated in time), thus increasing our understanding of the violent early stages of the Galaxy.

6 CONCLUSIONS

In this study we took advantage of the availability of high-quality astrometric, spectroscopic and asteroseismic data in order to explore how confidently we can apply asteroseismic inferences of metal poor stars for Galactic Archaeology. Our findings can be summarised as follows:

- Red giant ages from grid-based modelling are very sensitive to high-precision parallaxes such as those published by the Gaia Collaboration, at least in the parallax range represented in our sample. Hence, inaccuracies in parallax zero-point may result in shifts of several Gyr in modelled stellar ages, as the best fitting solutions may correspond to inaccurate distance moduli, resulting in an incorrect position in the HR diagram. For red giants with precise determinations of $\Delta\nu$ and ν_{\max} , the trade-off between accuracy and precision in age may result in a loss of accuracy when high-precision parallaxes are included, unless a very accurate calibration has been obtained for the parallax zero-point.
- However, the grid-based modelling results are not particularly sensitive to the code/grid adopted, at least for those tested here – BASTA/BaSTI and PARAM with models from Rodrigues et al. (2017). The choice of mass-loss parameter (zero mass-loss or $\eta = 0.3$) also did not have any significant effect in the results. However, this is not expected for red clump stars where mass-loss is relevant (Casagrande et al. 2016).
- Epstein et al. (2014) were correct when pointing out that the pure

asteroseismic scaling relations overestimate masses on the RGB, as already confirmed by several studies like those mentioned in Section 1. However, as seen in Fig. 5, the uncertainties resulting from grid-based modelling using the observables adopted by Epstein et al. (2014) and the corrections on the scaling relations still do not allow us to draw qualitative conclusions. In this work we confirm the required level of precision in the average asteroseismic parameters needed for APOKASC-2-level age precision using grid-based modelling. However, the differences in the results from APOKASC-2 and this work seen in Fig. 5 still need to be better understood. It is worth noting that the adoption of different metallicity values has a very mild effect in resulting masses and ages.

- There is a good amount of evidence for arguing that KIC 12017985 may be an evolved blue straggler. This object is a good target for long-term radial velocity monitoring, to check the possibility of a past mass transfer event that masked its initial mass, as well as to confirm (or rule out) that its large RUWE value published by Gaia is linked to binarity. From our results, only a mass transfer event from a former AGB companion can be ruled out, as there is no detection of extreme s-process enhancement. KIC 4671239 is an evolved blue straggler candidate as well, due to its low metallicity and young age, and there is tentative evidence of infrared excess, which might be the telltale sign of a relatively recent merger in this system. At the same time, their membership of unknown dwarfs recently accreted cannot be ruled out.

- KIC 6279038 exemplifies the sensitivity of the modelled fundamental parameters to the asteroseismic observables. Different published values of $\Delta\nu$ resulted in ages that would radically change the interpretation on the nature of this object. These results help to highlight the importance of a very careful inspection of the oscillation power spectra in a detailed analysis. This object would be useful to characterise the accreted population of Thamnos if it is confirmed as a member, being one of its oldest stars.

- Apart from KIC 4345370 and (maybe) the two blue straggler candidates, all stars are likely members of the accreted halo. Of those, only KIC 6279038 does not fit the age distribution of Gaia-Sausage (Montalbán et al. 2021), as well as being a potential member of Thamnos. A study with an expanded dataset that includes asteroseismic data for Sequoia and Thamnos could indicate the age distributions of these overdensities and clarify the status of KIC 8017159.

ACKNOWLEDGEMENTS

We thank the anonymous referee for important comments and suggestions. LC is the recipient of an ARC Future Fellowship (project number FT160100402). Parts of this research were conducted by the Australian Research Council Centre of Excellence for All Sky Astrophysics in 3 Dimensions (ASTRO 3D), through project number CE170100013. We also want to thank Zhen Yuan and GyuChul Myeong for kindly providing supporting data shown in Fig. 7. This research made use of astropy, <http://www.astropy.org>, a community-developed core python package for Astronomy (Astropy Collaboration et al. 2013, 2018), numpy (Harris et al. 2020), matplotlib (Hunter 2007), seaborn (Waskom 2021), scipy (Virtanen et al. 2020), Lightkurve, a python package for Kepler and TESS data analysis (Lightkurve Collaboration et al. 2018), and eche11e (Hey & Ball 2020). Some of the data presented herein were obtained at the W. M. Keck Observatory, which is operated as a scientific partnership among the California Institute of Technology, the University of California and the National Aeronautics and Space Administration. The Observatory was made possible by the generous

financial support of the W. M. Keck Foundation. The authors wish to recognize and acknowledge the very significant cultural role and reverence that the summit of Maunakea has always had within the indigenous Hawaiian community. We are most fortunate to have the opportunity to conduct observations from this mountain. This publication makes use of data products from the Two Micron All Sky Survey, which is a joint project of the University of Massachusetts and the Infrared Processing and Analysis Center/California Institute of Technology, funded by the National Aeronautics and Space Administration and the National Science Foundation.

DATA AVAILABILITY

The data underlying this article are available in the article and online through supplementary material.

REFERENCES

- Aguirre Børsen-Koch V., et al., 2021, arXiv e-prints, [p. arXiv:2109.14622](https://arxiv.org/abs/2109.14622)
- Alves-Brito A., Meléndez J., Asplund M., Ramírez I., Yong D., 2010, *A&A*, **513**, A35
- Amarsi A. M., Lind K., Asplund M., Barklem P. S., Collet R., 2016, *MNRAS*, **463**, 1518
- Anders F., et al., 2017, *A&A*, **597**, A30
- Astropy Collaboration et al., 2013, *A&A*, **558**, A33
- Astropy Collaboration et al., 2018, *AJ*, **156**, 123
- Baglin A., et al., 2006, in 36th COSPAR Scientific Assembly. p. 3749
- Bailer-Jones C. A. L., Rybizki J., Fouesneau M., Mantelet G., Andrae R., 2018, *AJ*, **156**, 58
- Bandyopadhyay A., Thirupathi S., Beers T. C., Susmitha A., 2020, *MNRAS*, **494**, 36
- Barbá R. H., Minniti D., Geisler D., Alonso-García J., Hempel M., Monachesi A., Arias J. I., Gómez F. A., 2019, *ApJ*, **870**, L24
- Barbuy B., et al., 2013, *A&A*, **559**, A5
- Bayo A., Rodrigo C., Barrado Y Navascués D., Solano E., Gutiérrez R., Morales-Calderón M., Allard F., 2008, *A&A*, **492**, 277
- Belokurov V., Erkal D., Evans N. W., Koposov S. E., Deason A. J., 2018, *MNRAS*, **478**, 611
- Belokurov V., et al., 2020, *MNRAS*, **496**, 1922
- Bennett M., Bovy J., 2019, *MNRAS*, **482**, 1417
- Binney J., 2012, *MNRAS*, **426**, 1324
- Blackwell D. E., Shallis M. J., 1977, *MNRAS*, **180**, 177
- Bovy J., 2015, *ApJS*, **216**, 29
- Brogaard K., et al., 2018, *MNRAS*, **476**, 3729
- Brown T. M., Gilliland R. L., Noyes R. W., Ramsey L. W., 1991, *ApJ*, **368**, 599
- Casagrande L., 2016, Unveiling the origin of the young [alpha/Fe]-rich stars, Keck Observatory Archive HIRES Z079Hr
- Casagrande L., 2020, *ApJ*, **896**, 26
- Casagrande L., Ramírez I., Meléndez J., Bessell M., Asplund M., 2010, *A&A*, **512**, A54
- Casagrande L., et al., 2014, *ApJ*, **787**, 110
- Casagrande L., et al., 2016, *MNRAS*, **455**, 987
- Casagrande L., et al., 2021, *MNRAS*, **507**, 2684
- Castelli F., Kurucz R. L., 2003, in Piskunov N., Weiss W. W., Gray D. F., eds, IAU Symposium Vol. 210, Modelling of Stellar Atmospheres. p. 20P
- Cayrel R., et al., 2004, *A&A*, **416**, 1117
- Chaplin W. J., Miglio A., 2013, *ARA&A*, **51**, 353
- Chaplin W. J., et al., 2011, *Science*, **332**, 213
- Cutri R. M., et al., 2003, 2MASS All Sky Catalog of point sources.
- Cutri R. M., et al., 2014, VizieR Online Data Catalog, [p. II/328](https://vizier.cesr.cnrs.fr/vizieR)
- De Silva G. M., et al., 2015, *MNRAS*, **449**, 2604
- Di Matteo P., Haywood M., Lehnert M. D., Katz D., Khoperskov S., Snaith O. N., Gómez A., Robichon N., 2019, *A&A*, **632**, A4
- El-Badry K., Rix H.-W., Heintz T. M., 2021, *MNRAS*, **506**, 2269
- Epstein C. R., Johnson J. A., Dong S., Udalski A., Gould A., Becker G., 2010, *ApJ*, **709**, 447
- Epstein C. R., et al., 2014, *ApJ*, **785**, L28
- Fabrizius C., et al., 2021, *A&A*, **649**, A5
- Feuillet D. K., Feltzing S., Sahlholdt C. L., Casagrande L., 2020, *MNRAS*, **497**, 109
- Freeman K., Bland-Hawthorn J., 2002, *ARA&A*, **40**, 487
- Gaia Collaboration et al., 2018, *A&A*, **616**, A1
- Gaia Collaboration et al., 2021, *A&A*, **649**, A1
- Gaulme P., et al., 2016, *ApJ*, **832**, 121
- Gilmore G., et al., 2012, *The Messenger*, **147**, 25
- Green G. M., Schlafly E., Zucker C., Speagle J. S., Finkbeiner D., 2019, *ApJ*, **887**, 93
- Harris C. R., et al., 2020, *Nature*, **585**, 357
- Haywood M., Di Matteo P., Lehnert M. D., Snaith O., Khoperskov S., Gómez A., 2018, *ApJ*, **863**, 113
- Hekker S., Christensen-Dalsgaard J., 2017, *A&ARv*, **25**, 1
- Helmi A., 2020, *ARA&A*, **58**, 205
- Hey D., Ball W., 2020, Echelle: Dynamic echelle diagrams for asteroseismology, [doi:10.5281/zenodo.3629933](https://doi.org/10.5281/zenodo.3629933), <https://doi.org/10.5281/zenodo.3629933>
- Hidalgo S. L., et al., 2018, *ApJ*, **856**, 125
- Hinkle K., Wallace L., Valenti J., Harmer D., 2000, Visible and Near Infrared Atlas of the Arcturus Spectrum 3727-9300 A
- Howell S. B., et al., 2014, *PASP*, **126**, 398
- Hunter J. D., 2007, *Computing in Science & Engineering*, **9**, 90
- Ishigaki M. N., Aoki W., Chiba M., 2013, *ApJ*, **771**, 67
- Jean-Baptiste I., Di Matteo P., Haywood M., Gómez A., Montuori M., Combes F., Semelin B., 2017, *A&A*, **604**, A106
- Jofré P., Heiter U., Soubiran C., 2019, *Annual Review of Astronomy and Astrophysics*, **57**, 571
- Jönsson H., et al., 2020, *AJ*, **160**, 120
- Kippenhahn R., Weigert A., Weiss A., 2012, Stellar Structure and Evolution, [doi:10.1007/978-3-642-30304-3](https://doi.org/10.1007/978-3-642-30304-3).
- Kjeldsen H., Bedding T. R., 1995, *A&A*, **293**, 87
- Kobayashi C., Nakasato N., 2011, *ApJ*, **729**, 16
- Kobayashi C., Karakas A. I., Lugaro M., 2020, *ApJ*, **900**, 179
- Koch D. G., et al., 2010, *ApJ*, **713**, L79
- Koppelman H., Helmi A., Veljanoski J., 2018, *ApJ*, **860**, L11
- Koppelman H. H., Helmi A., Massari D., Price-Whelan A. M., Starkeburg T. K., 2019, *A&A*, **631**, L9
- Lightkurve Collaboration et al., 2018, Lightkurve: Kepler and TESS time series analysis in Python, Astrophysics Source Code Library ([ascl:1812.013](https://arxiv.org/abs/1812.013))
- Limberg G., et al., 2021, *ApJ*, **907**, 10
- Lind K., Bergemann M., Asplund M., 2012, *MNRAS*, **427**, 50
- Lindgren L., et al., 2021, *A&A*, **649**, A4
- Mackereth J. T., Bovy J., 2018, *PASP*, **130**, 114501
- Majewski S. R., et al., 2017, *AJ*, **154**, 94
- Matteucci F., Greggio L., 1986, *A&A*, **154**, 279
- McMillan P. J., 2017, *MNRAS*, **465**, 76
- McWilliam A., 1997, *ARA&A*, **35**, 503
- Meléndez J., et al., 2012, *A&A*, **543**, A29
- Miglio A., et al., 2012, *MNRAS*, **419**, 2077
- Miglio A., et al., 2016, *MNRAS*, **461**, 760
- Montalbán J., et al., 2021, *Nature Astronomy*,
- Monty S., Venn K. A., Lane J. M. M., Lokhorst D., Yong D., 2020, *MNRAS*, **497**, 1236
- Mosser B., et al., 2014, *A&A*, **572**, L5
- Mosser B., Gehan C., Belkacem K., Samadi R., Michel E., Goupil M. J., 2018, *A&A*, **618**, A109
- Myeong G. C., Evans N. W., Belokurov V., Sanders J. L., Koposov S. E., 2018, *ApJ*, **863**, L28
- Myeong G. C., Vasiliev E., Iorio G., Evans N. W., Belokurov V., 2019, *MNRAS*, **488**, 1235
- Nomoto K., Kobayashi C., Tominaga N., 2013, *ARA&A*, **51**, 457
- Pinsonneault M. H., et al., 2014, *ApJS*, **215**, 19
- Pinsonneault M. H., et al., 2018, *ApJS*, **239**, 32

Planck Collaboration et al., 2016, *A&A*, 594, A20
 Planck Collaboration et al., 2020, *A&A*, 641, A6
 Ricker G. R., et al., 2014, in Oschmann Jacobus M. J., Clampin M., Fazio G. G., MacEwen H. A., eds, Society of Photo-Optical Instrumentation Engineers (SPIE) Conference Series Vol. 9143, Space Telescopes and Instrumentation 2014: Optical, Infrared, and Millimeter Wave. p. 914320 ([arXiv:1406.0151](https://arxiv.org/abs/1406.0151)), doi:10.1117/12.2063489
 Rodrigues T. S., et al., 2014, *MNRAS*, 445, 2758
 Rodrigues T. S., et al., 2017, *MNRAS*, 467, 1433
 Salaris M., Chieffi A., Straniero O., 1993, *ApJ*, 414, 580
 Schönrich R., Binney J., Dehnen W., 2010, *MNRAS*, 403, 1829
 Searle L., Zinn R., 1978, *ApJ*, 225, 357
 Serenelli A., et al., 2017, *ApJS*, 233, 23
 Sharma S., Stello D., Bland-Hawthorn J., Huber D., Bedding T. R., 2016, *ApJ*, 822, 15
 Silva Aguirre V., et al., 2015, *MNRAS*, 452, 2127
 Silva Aguirre V., et al., 2017, *ApJ*, 835, 173
 Silva Aguirre V., et al., 2018, *MNRAS*, 475, 5487
 Silva Aguirre V., et al., 2020, *ApJ*, 889, L34
 Sneden C. A., 1973, PhD thesis, THE UNIVERSITY OF TEXAS AT AUSTIN.
 Soderblom D. R., 2010, *ARA&A*, 48, 581
 Stello D., et al., 2009, *ApJ*, 700, 1589
 Stello D., et al., 2014, *ApJ*, 788, L10
 Tailo M., et al., 2020, *MNRAS*, 498, 5745
 Ting Y.-S., Hawkins K., Rix H.-W., 2018a, *ApJ*, 858, L7
 Ting Y.-S., Hawkins K., Rix H.-W., 2018b, *ApJ*, 864, L39
 Tinsley B. M., 1979, *ApJ*, 229, 1046
 Tolstoy E., Hill V., Tosi M., 2009, *ARA&A*, 47, 371
 Ulrich R. K., 1986, *ApJ*, 306, L37
 Valentini M., et al., 2019, *A&A*, 627, A173
 Venn K. A., Irwin M., Shetrone M. D., Tout C. A., Hill V., Tolstoy E., 2004, *AJ*, 128, 1177
 Verma K., Grand R. J. J., Silva Aguirre V., Stokholm A., 2021, *MNRAS*, 506, 759
 Virtanen P., et al., 2020, *Nature Methods*, 17, 261
 Vogt S. S., et al., 1994, in Crawford D. L., Craine E. R., eds, Society of Photo-Optical Instrumentation Engineers (SPIE) Conference Series Vol. 2198, Instrumentation in Astronomy VIII. p. 362, doi:10.1117/12.176725
 Waskom M. L., 2021, *Journal of Open Source Software*, 6, 3021
 White S. D. M., Rees M. J., 1978, *MNRAS*, 183, 341
 Yong D., et al., 2014, *MNRAS*, 439, 2638
 Yong D., et al., 2016, *MNRAS*, 459, 487
 Yu J., Huber D., Bedding T. R., Stello D., Hon M., Murphy S. J., Khanna S., 2018, *ApJS*, 236, 42
 Yuan Z., et al., 2020, *ApJ*, 891, 39
 Zinn J. C., 2021, *AJ*, 161, 214
 Zinn J. C., Pinsonneault M. H., Huber D., Stello D., 2019a, *ApJ*, 878, 136
 Zinn J. C., Pinsonneault M. H., Huber D., Stello D., Stassun K., Serenelli A., 2019b, *ApJ*, 885, 166
 Zinn J. C., et al., 2020, *ApJS*, 251, 23
 Zinn J. C., et al., 2021, arXiv e-prints, p. arXiv:2108.05455
 da Silva L., et al., 2006, *A&A*, 458, 609

Table A1. Internal uncertainties of the atmospheric parameters from Table 3, calculated as described in Section 3.1.1. The last column also shows the S/N for the spectrum of each target.

Star	σT_{eff} K	$\sigma \log g$ dex	$\sigma [M/H]$ dex	σv_t km s ⁻¹	S/N @590nm
KIC4345370	71	0.004	0.04	0.04	130
KIC4671239	145	0.002	0.11	0.09	57
KIC6279038	79	0.020	0.06	0.11	85
KIC7191496	96	0.007	0.08	0.18	75
KIC8017159	58	0.003	0.05	0.14	165
KIC11563791	56	0.005	0.03	0.09	95
KIC12017985	90	0.007	0.06	0.06	170

APPENDIX A: SOME EXTRA MATERIAL

This paper has been typeset from a $\text{\TeX}/\text{\LaTeX}$ file prepared by the author.

Table A2. Internal uncertainties, in dex, of the 'absolute' abundance A(X) for each species X.

Star	O	Na	Mg	Al	Si	Ca	Sc	Ti	V	Cr	Mn	FeI	FeII
KIC4345370	0.06	0.11	0.08	0.08	0.02	0.11	0.06	0.09	0.13	0.06	0.10	0.11	0.07
KIC4671239	0.07	0.10	...	0.19	0.20	...
KIC6279038	0.03	...	0.06	0.12	0.02	0.17	0.13	...	0.14	0.17	0.16
KIC7191496	0.17	0.04	0.19	0.21	0.12
KIC8017159	0.03	...	0.05	...	0.03	0.16	0.07	0.26	0.10	0.18	0.13
KIC11563791	0.04	0.10	0.11	...	0.08	0.09	0.06	0.15	0.10	0.04	0.10	0.12	0.15
KIC12017985	0.11	0.05	0.06	...	0.03	0.13	0.08	0.15	0.16	...	0.09	0.17	0.17
	Co	Ni	Cu	Zn	Sr	Y	Zr	Ba	La	Ce	Nd	Sm	Eu
KIC4345370	0.06	0.14	0.08	0.07	0.12	0.17	0.16	0.14	0.08	0.17	0.20	0.05	0.03
KIC4671239
KIC6279038	...	0.09	0.15	0.04	...	0.08	...	0.05	0.10	0.03	0.07	0.13	...
KIC7191496	...	0.12	...	0.05	...	0.09	...	0.05
KIC8017159	...	0.08	...	0.11	...	0.07	0.01	0.04	0.06	...	0.07
KIC11563791	...	0.13	0.07	0.22	...	0.06	...	0.15	0.04	...	0.10	0.03	0.05
KIC12017985	...	0.08	0.09	0.04	...	0.08	...	0.06	0.09	0.05	0.12	...	0.02